Detection of intra-band gap defects states in spin-coated sol-gel SnO_x nanolayers by photoelectron spectroscopies

OPEN ACCESS
IOP Publishing
Journal of Physics D: Applied Physics
J. Phys. D: Appl. Phys. **51** (2018) 315301 (9pp)
https://doi.org/10.1088/1361-6463/aacf3a

Detection of intra-band gap defects states in spin-coated sol-gel SnO_x nanolayers by photoelectron spectroscopies

Lucyna Grządziel[1], Maciej Krzywiecki[1,2], Anna Szwajca[3], Adnan Sarfraz[2], Georgi Genchev[2] and Andreas Erbe[2,4]

[1] Institute of Physics—Center for Science and Education, Silesian University of Technology, S. Konarskiego Str. 22B, 44-100 Gliwice, Poland
[2] Max-Planck-Institut für Eisenforschung GmbH, Max-Planck-Str. 1, 40237 Düsseldorf, Germany
[3] Faculty of Chemistry, Adam Mickiewicz University in Poznań, Umultowska Str. 89 b, 61-614 Poznań, Poland
[4] Department of Materials Science and Engineering, NTNU, Norwegian University of Science and Technology, 7491 Trondheim, Norway

E-mail: Maciej.Krzywiecki@polsl.pl

Received 17 April 2018, revised 19 June 2018
Accepted for publication 26 June 2018
Published 11 July 2018

Abstract

The presence of occupied intra-band gap states in oxygen-deficient tin dioxide (SnO_x; $1 < x < 2$) is crucial for efficient manufacturing of multipurpose electronic devices based on transparent conducting oxides. Former experimental determination of these states was conducted for well-defined, usually thick tin oxides obtained under highly controlled vacuum conditions. In this work, we present precise specification of gap defects states for ultra-thin SnO_x layers prepared by sol-gel synthesis followed with spin-coat deposition. Post-deposition drying and annealing processing changed layers' surface morphology and bulk crystalline structure as monitored by scanning electron microscopy, atomic force microscopy and x-ray diffraction. An x-ray photoemission spectroscopy (XPS) analysis of chemical composition revealed the presence of both Sn^{2+} and Sn^{4+} species in layers with and without post-drying annealing step. A stronger contribution of SnO was found for dried SnO_x. In the valence band region, XPS studies revealed pronounced O 2p and hybridised Sn 5p/5s–O 2p states as well as deep, overlapping with the O 2p, band gap states resulting from Sn 5s orbitals. These states—attributed to defect states—indicated enhanced presence of Sn^{2+} cations, and were assigned to 'bridging' oxygen vacancies. Complementary photoemission yield spectroscopy (PYS) studies of the SnO_x band gap region revealed an increased effective density of occupied electronic states below the Fermi level E_F for annealed layers. The consequence was a work function reduction by 0.15 eV after the annealing process. PYS results allowed a precise detection of SnO_x shallow band gap states close to E_F. These states were attributed to surface oxygen vacancies, which was confirmed by computer modelling. Finally, the annealed layers exhibited higher calculated charge carrier concentration, hence the increased n-type character.

Keywords: tin oxides, band gap states, defect states, oxygen vacancies, photoemission spectroscopies

(Some figures may appear in colour only in the online journal)

Introduction

Tin oxides, due to their tuneable electrical, electronic and optical properties, are permanently attracting attention of scientists and technologists. Especially tin(IV)-oxide (SnO_2), exhibiting high electrical conductivity and transparency, has become a key material for various optoelectronic device technologies as transparent conducting oxide (TCO) or gas sensing layer [1–4]. Due to an insufficient number of carriers, it is rarely applied in its pure stoichiometric form SnO_2 as a semiconductor with wide band gap E_g of 3.6 eV [1, 5]. However, intrinsic defects originating from oxygen deficiency or impurity dopants lead to deviations from the ideal stoichiometry, designated here as SnO_x ($1 < x < 2$). The concomitant higher conductivity is desired e.g. for application as TCO. The presence of crystallographic imperfections and additives leads to the creation of additional occupied electronic states, preferentially surface states, in the band gap, affecting the energy position of the Fermi level E_F, and charge carrier concentration [6–8].

Many experimental and theoretical studies have focused on determination of surface defects states of SnO_x, but their results are debated, as they appear to be strongly dependent on the particular stoichiometry and conditions of oxide production [1, 9–11]. Even for the same oxide stoichiometry, surface structure and phase composition may depend on the preparation technique [1]. Likewise, oxide electronic structure is strongly affected by coexisting dual valency of the tin cations, preferably forming an oxidation state of +4 or +2 [1].

One of the most useful experimental methods allowing electronic and chemical structure description is the set of photoemission techniques, comprising ultraviolet and x-ray photoemission spectroscopies (UPS and XPS, respectively). For tin oxides, XPS studies focused mainly on [O]/[Sn] ratio estimation, determination of tin valencies and their evolution during external processes, e.g. ion bombardment, whereas UPS investigations concerned modification of valence band (VB) and shallow core levels in terms of bulk density of states (DOS) induced by surface treatment [12–14]. The majority of recent studies was conducted for well-defined samples in form of thick layers. However, future applications demand cheaper technologies which often produce less defined samples with electronic properties which are still not well understood and described. Contrary to tin oxide layers obtained in highly controlled vacuum conditions by epitaxial growth [15], magnetron sputtering [16], laser-induced chemical vapour deposition [17], rheotaxial growth and thermal or vacuum oxidation [18, 19], SnO_x thin films can be also prepared using sol-gel synthesis connected with e.g. spin-coat deposition. This simple, low-cost technology ensures sufficient control of deposition parameters under ambient conditions. It is simultaneously attractive for mass production of optoelectronic elements.

In this work, we present an approach to tune the electronic properties of sol-gel derived SnO_2 layers with extreme oxygen deficiency by simple post-deposition treatments like drying or annealing. We show that besides changes reflected in surface morphology and bulk structure monitored by scanning electron microscopy (SEM), atomic force microscopy (AFM) and x-ray diffraction (XRD) respectively, the alterations touch in a subtle manner the near valence band energy region of the material. We focused on detection of band gap defects states utilizing both traditional XPS and unconventional fine-resolved photoemission yield spectroscopy (PYS), a technique comparable to UPS. PYS operates with photon energies between 3 and 6 eV. Hence, the mean free path of photoelectrons reaches 10 nm, allowing for investigation of semiconductor space charge layers with extremely limited impact of final state effects [20]. Moreover, due to an excellent sensitivity and energy resolution of 0.03 eV, PYS enables accurate revelation of energy level positions including E_F and the top of VB, E_V. An additional advantage of PYS is the possibility of precise determination of effective density of occupied electronic states localized in the band gap below E_F, as well as in the upper part of the VB [21–23]. Based on PYS analysis supported by DOS theoretical calculations, experimental determination of occupied electronic states close to E_F was executed.

Materials and methods

The SnO_x layers were prepared by a sol-gel technique and deposited by spin-coating. As substrates, silicon Si(1 0 0) wafers (SiMat, n-type, P-doped, 5–10 $\Omega \cdot$ cm) covered by native oxide were used. For cleaning, substrates were ultrasonicated sequentially in acetone, isopropanol, and de-ionized water for 15 min per medium. Then, the substrates were blown dry with a N_2 stream and further dried in a furnace under air atmosphere for 30 min at 110 °C. The 0.025 M SnO_x sol was prepared by mixing tin(IV) isopropoxide with triethylamine (TEA) in a molar ratio of 1:1, and subsequently diluting with isopropanol. All reagents were supplied by VWR International and used as purchased. Prior to sol deposition, the substrates were functionalized by rinsing with 0.007 M TEA in isopropanol and then immediately dried with a N_2 stream. The spin-coat deposition process (Spin-coater P6700, Specialty Coating Systems Inc.) was conducted in four cycles with the following recipe per cycle: 500 rpm for 2 s, 2000 rpm for 8 s and 6000 rpm for 20 s. After each cycle, samples were dried in air for 10 min at 110 °C resulting in the series of SnO_x layers referred to as 'dried'. Subsequently, a selection of the samples were additionally annealed after the deposition process in a tube furnace at 550 °C for 4 h in ambient atmosphere. These samples will be referred to as 'annealed'. The layer thicknesses were estimated as close to 12 nm utilizing angle-dependent XPS measurements and calculation procedures with details described elsewhere [7].

The surface morphology of the layers was performed by SEM (Carl Zeiss LEO 1550 VP) with an in-lens detector (working distance: 3 mm; ETH voltage: 15 kV).

Additionally, surface topography was investigated by AFM using a PSIA XE-70 microscope in non-contact (NC-AFM) mode. BS Tap300Al cantilevers (resonance frequency 300 kHz, spring constant 40 $N \cdot m^{-1}$) were applied. Recorded images were processed using image processing software (WSxM5.0®) [24] to compensate sample inclination and distortions caused by the z-scanning stage. All quantitative

topography related analyses were conducted applying WSxM built-in algorithms. Surface roughness was quantified by root mean square (RMS) deviation from a planar surface.

For bulk structure characterization, the XRD was employed using a Bruker-AXS D8 with Cu-K_α source of wavelength 0.154 nm.

The XPS investigation was carried out with a Physical Electronics PHI Quantera II spectrometer equipped with an Al-K_α micro-focused source and a dual-beam charge neutralizer. The survey spectra were recorded with an energy step of 0.4 eV and the pass energy set to 140 eV. The individual core level spectra were recorded with 0.025 eV energy step and 26 eV pass energy. The XPS system base pressure was kept at 9×10^{-8} Pa. All XPS spectra were recorded with 45° take-off angle. The XPS data were analysed by curve fitting using CASA XPS® software [25]. If not specified otherwise in the text, each peak was represented by a product of a Gaussian (70%) and a Lorentzian (30%) line. The secondary electron background was subtracted with a Shirley function. The full width at half maximum (FWHM) of the components at the same energy region were allowed to vary within a narrow range. The lowest possible number of components were used that yielded acceptably low residual values. The uncertainty estimated for a particular component energy position determination was 0.07 eV. Quantitative analysis, e.g. component ratio determination, was done with use of CASA XPS® embedded relative sensitivity factors and algorithms [25]. The binding energy (BE) scale was calibrated to Au $4f_{7/2}$ (84.0 eV) recorded for a gold plate placed in the same sample holder [23].

PYS was also measured under ultra-high vacuum conditions (system base pressure 7.5×10^{-8} Pa). The samples were irradiated with ultraviolet light from a deuterium source connected to a Zeiss™ monochromator and a fibre-based optical path. Excitation wavelength varied in the range of 200–400 nm with step of 1 nm, which corresponded to photon energy of 3.1–6.2 eV with a resolution better than 0.03 eV at room temperature. The spectral intensity of light was monitored by a Rohre M12FQC51 photomultiplier. The photoemission yield spectra $Y(E)$ were collected using a spectrometer containing a Hamamatsu channeltron electron multiplier and a SemiInstruments™ acquisition setup. Derivatives of $Y(E)$ spectra with respect to photon energy were calculated in order to obtain the effective density of occupied electronic states $N(E)$ localized below the Fermi level in the band gap [21]. The quantitative PYS data analysis was performed by peak fitting procedure embedded in OriginLab® v8.5 software. Particular PYS energy regions were decomposed by curve-fitting procedure with Gaussian (100%) lines after background subtraction.

Computation of the electronic structure were executed by a semi-empirical calculation with a method based on the AM1/d Hamiltonian (MO-G Version 1.1, Fujitsu Limited, Tokyo, Japan, 2008) using the Scigress software (Fujitsu Ltd) on a Windows workstation. As representation of SnO_x geometry, cluster structures were constructed consisting of 19 or 17 oxygen atoms and 18 Sn atoms. The proposed structures were fully optimized using the Gaussian03 program package without any symmetry restrictions utilizing the B3LYP level of theory by using the LanL2DZ basis set [26]. The Sn–O bonds in nanostructures had distances of 2.078 Å (average value). The GaussSum 3.0 was applied to calculate group contributions to the molecular orbitals. The DOS spectra were created by convoluting the molecular orbital information with Gaussian curves of unit height and FWHM of 0.3 eV [27].

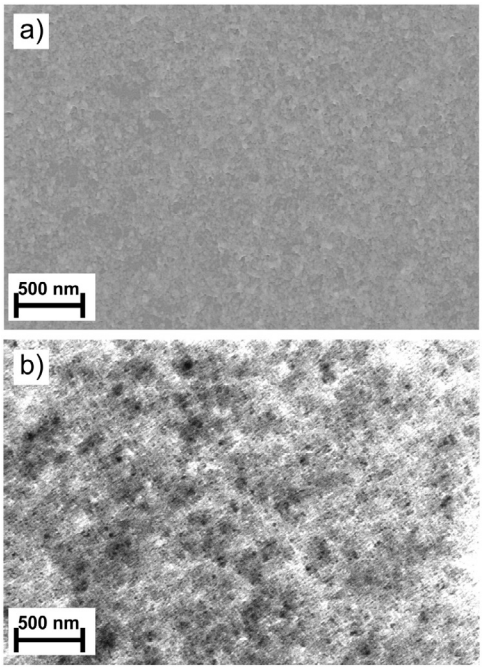

Figure 1. SEM images of surfaces after deposition of dried (a) and annealed (b) SnO_x layers.

Results and discussion

SEM images in figure 1 show the surface morphology of dried (figure 1(a)) and annealed (figure 1(b)) SnO_x thin layers. The image of the dried layer shows nearly amorphous and uniform topography with slightly visible, small grains. Contrary to the dried layer, the image of the annealed layer surface exhibits more developed crystallites uniformly distributed but without clear, preferential ordering with respect to the substrate plane. Dark spots and light bands visible on the annealed oxide image aside from topographical attributes can also represent reduced or enhanced density of charge stimulated by the electron beam during SEM image acquisition. Thus, microscopic examination of the layers revealed a strong impact of the post-deposition annealing on the layer morphology.

For quantification of surface topography features, the NC-AFM imaging of surface topography of dried and annealed samples was conducted. Obtained images are shown in figures 2(a) and (b), respectively. The images confirmed differences in degree of crystallization between samples, revealing more separated, developed grains with uniform geometry on annealed SnO_x surface. This trend supported roughness analysis histograms associated with AFM images where distribution of grain height for annealed layer (figure 2(d)) is significantly narrower than for dried one (figure 2(c)) pointing

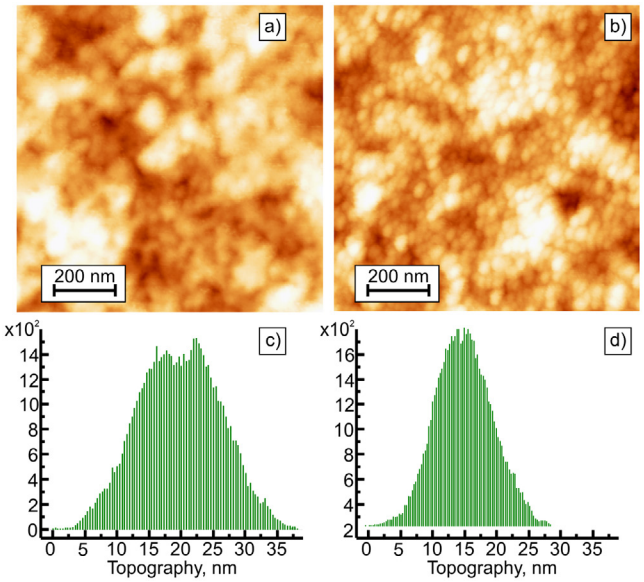

Figure 2. NC-AFM images (1 μm × 1 μm) of SnO_x surfaces for dried (a) and annealed (b) layers. Each image is accompanied by roughness analysis histogram ((c) and (d), correspondingly) demonstrating the number of events as a function of their height.

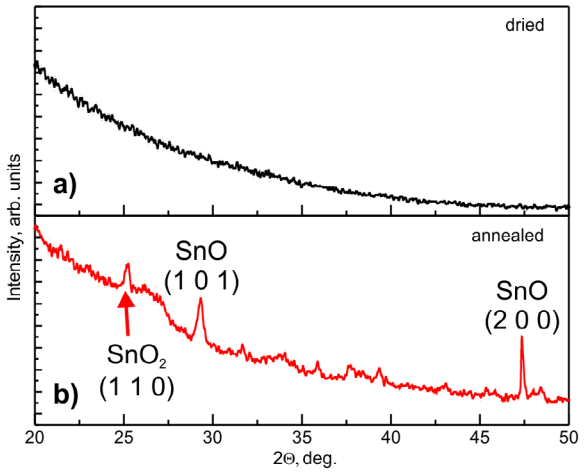

Figure 3. XRD patterns for dried (a) and annealed (b) SnO_x layers. Increasing background at low angles is an instrument-related feature and is not related to scattering from disordered structure.

out more established topography. To quantify surface features of samples, the RMS roughness was determined as 6.3(2) nm and 4.4(2) nm for dried and annealed layer, respectively.

To determine how post-deposition processes affect bulk structure, XRD studies were conducted. Figure 3 presents the XRD patterns for both kinds of layers. The diffractogram of the dried film (figure 3(a)) displays no traces of distinct peaks, indicating amorphous composition of bulk layers. The XRD pattern of the post-deposition annealed layer (figure 3(b)) displays at least three very distinctive peaks at the diffraction angles 2θ close to 25°, 29° and 47°. These angles correspond to co-existing crystallographic phases from SnO_2 and SnO with significant reflections SnO_2 (1 1 0), SnO (1 0 1), and SnO (2 0 0), respectively [28–30]. Further peaks with low intensity were also present. The XRD results coincide well to the statements derived from surface microscopic studies and confirms the mostly amorphous character of dried layers and the more crystalline character of those that were annealed.

Similar results were reported earlier in the literature for sputtered SnO_x thin films, when the increase of substrate temperature led to morphological changes simultaneously associated with stoichiometry variation [31, 32]. Sputtered tin oxides with substrate temperature lower than 100 °C (roughly corresponding to drying conditions of our samples), exhibited an amorphous and highly oxygen-deficient SnO_x phase with embedded nanocrystalline SnO_2 grains [31, 32]. Heating them up to 600 °C (as analogy condition of our annealing process) caused forming of large SnO_2 grains surrounded by shrunken SnO phase, consequently modifying oxygen substoichiometry [33–35].

In order to check the impact of post-deposition processes on the chemical composition and stoichiometry, XPS was conducted. Figure 4 shows O 1s, Sn $3d_{5/2}$ and C 1s energy regions for dried and annealed samples (figures 4(a)–(c), respectively). For both kinds of layers, the decomposition of the O 1s peak revealed prominent component assigned to an O–Sn bond and a noticeable one derived from residual organic contaminants ($O_{cont.}$). The relatively significant intensity of $O_{cont.}$ component originates from the surface placement of the adsorbate layer which is consistent with C 1s analysis described further. Minor traces of a particular contaminant was found for dried SnO_x and attributed to O–C bond probably related to ambience-layer interaction. This component was not visible in annealed sample's spectrum.

Decomposition of the Sn $3d_{5/2}$ peak showed two major components originating from Sn^{2+} and Sn^{4+} for dried and annealed layer. Chemical shift between these ionic species in the order of 0.6 eV was determined coinciding with results of XPS characterisation of tin oxides conducted by Themlin *et al* [12]. Small trace of Sn^0 was also detected, with intensity significantly bigger in the case of dried SnO_x. Applying the procedure described in [12], the concentration ratio of $[Sn^{2+}]/([Sn^0] + [Sn^{2+}] + [Sn^{4+}])$ was estimated as equal to 0.325(7) and 0.314(7) for dried and annealed samples, respectively. These values show a stronger change of oxidation state from Sn^{4+} to Sn^{2+} in the dried layer [12]. Moreover, for both O 1s and Sn $3d_{5/2}$ major components, an energy shift of peak maximum position of about 0.5 eV was observed toward higher BE for the annealed layer compared to the dried one. Finally, calculating [O]/[Sn] elemental ratio to estimate x in SnO_x yielded values of 1.03(1) and 1.08(1) for dried and annealed samples, respectively, manifesting nearly similar oxygen substoichiometry with stronger fraction of the SnO-like environment in the dried layer.

The C 1s energy region (figure 4(c)) depicts contributions of contaminating organic components to the sol-gel prepared SnO_x. The peak decomposition reveals components assigned to C–C, C–OH (alternatively C–C–O), and C–O. These components originate from residues of the precursors, and from ambience-layer interaction [36–38]. Post-deposition annealing significantly reduced the C–C and C–OH components. This reduction could either be caused by evaporation of residual organic solvents, or chemical decomposition of residual precursor alkoxides during annealing. Also the C–O

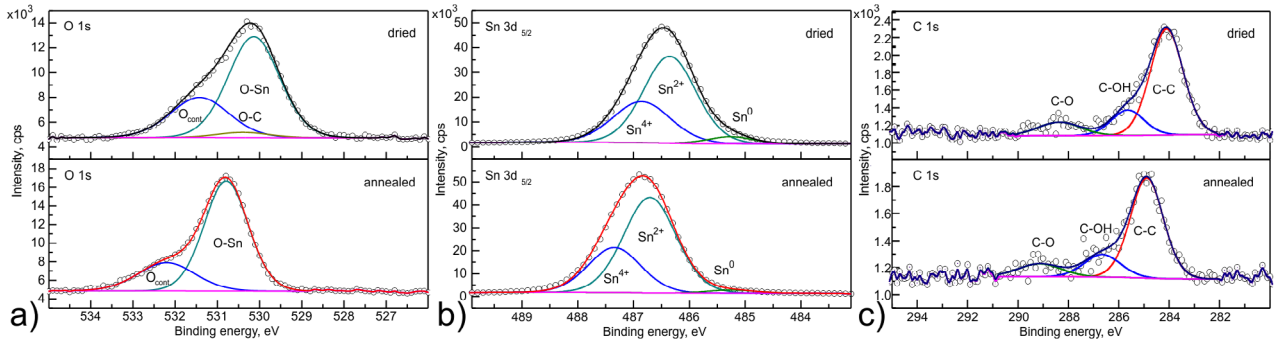

Figure 4. XPS energy regions of O 1s (a), Sn $3d_{5/2}$ (b) and C 1s (c) core levels for dried and annealed SnO_x layers as indicated in the respective panel. Note the significant difference in intensity scale (*y*-axis) in the case of the C 1s region.

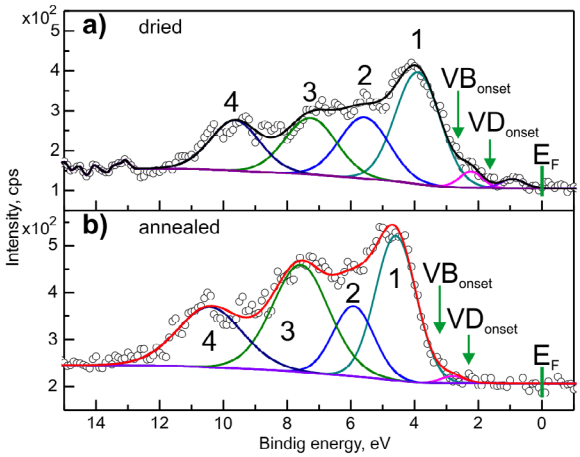

Figure 5. The XPS spectrum of VB and band gap region for dried (a) and annealed (b) SnO_x layers. Components of the complex peak have been labelled 1, 2, 3 and 4. Assignment is discussed in the text.

component reduced in intensity during annealing, which corresponds with results of O 1s analysis of organic components. Nevertheless, the impact of carbon-related contaminants on layers' chemical composition can be treated as negligible taking into account the weak C 1s signal in comparison to the distinct peaks in the O 1s and Sn $3d_{5/2}$ energy regions, with a nearly 10:1 signal ratio after sensitivity factor correction.

Figure 5 shows XPS results for VB and band gap region below E_F. Recorded spectra for both layers revealed main components corresponding to O 2p states as well as to Sn 5p–O 2p and Sn 5s–O 2p hybridised states (peaks 1, 3 and 4, respectively) [1, 12]. An additional trace of carbonaceous species-related states (peak no. 2) is also apparent [39]. As the O 2p peak onset (VB_{onset}) indicated E_V, the energy distance $E_V - E_F$ was determined as equalling 2.55(7) eV and 3.05(7) eV for dried and annealed oxides, respectively. The 0.5 eV energy shift of valence band edge between dried and annealed layers corresponds to the detected energy shift of O 1s and Sn 3d components. It should be pointed out that precise determination of the E_V position was complicated because of appearance of additional, overlapping peak situated at lower BE. This component was interpreted as deep band gap states generally assigned to SnO_x-related defect levels (VD) [23]. These defect states are induced mainly by oxygen deficiencies, leading to a transformation of stoichiometric Sn^{4+} valency into Sn^{2+} [1].

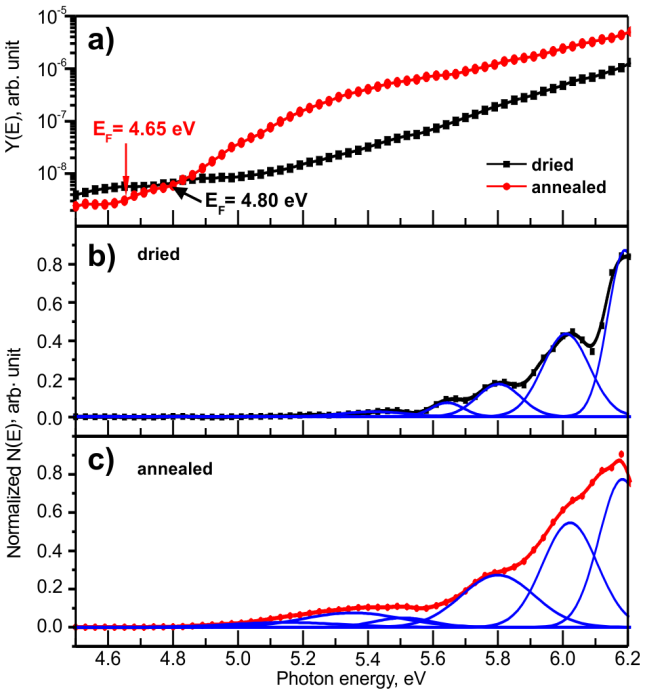

Figure 6. PYS spectra $Y(E)$ for dried and annealed SnO_x layers on a semilogarithmic scale (a). Derived effective density of occupied electronic states $N(E)$ localized in the band gap below E_F with particular components of dried (b) and annealed (c) layers.

Enhanced occurrence of Sn^{2+} cations caused deep band gap emission of Sn 5s electrons overlapping with the low binding energy tail of the O 2p signal as observed before by Themlin *et al* [12] and Batzill *et al* [1] during XPS studies of reduced-SnO_2 surfaces. Formation of defect states in the band gap near E_V were also reported by Cox *et al* [13] for a nearly pure SnO_2 crystal subjected to UPS investigations. The authors pointed out the origin of these states as result of reduction of Sn^{4+} to Sn^{2+} species arising from 'bridging' oxygen vacancies [13].

Following the procedure described in [12], the peak intensity ratio $I_{Sn\ 5s}/I_{O\ 2p}$ was estimated as 0.08(2) and 0.03(2), respectively, for dried and annealed samples. Higher value of the $I_{Sn\ 5s}/I_{O\ 2p}$ ratio distinctly indicated increased concentration of Sn^{2+} species for dried SnO_x which is consistent with deep energy level examination. Furthermore, the low BE edge of VD_{onset} was located 1.70 eV and 2.46 eV, respectively, from E_F, which was 0.85 eV and 0.59 eV, respectively, from

Table 1. Energy positions of components in the effective density of filled state $N(E)$ on an absolute energy scale ($E_{vac} = 0$ eV) and on the BE scale ($E_F = 0$ eV) with corresponding FWHM values for dried and annealed SnO_x obtained from PYS experiments.

SnO_x	Absolute energy (eV)	Binding energy (eV)	FWHM (eV)
Dried	5.42	0.62	0.24
	5.64	0.84	0.12
	5.80	1.00	0.16
	6.01	1.21	0.17
	6.19	1.39	0.16
Annealed	5.14	0.49	0.40
	5.35	0.70	0.35
	5.51	0.86	0.21
	5.80	1.15	0.27
	6.02	1.37	0.20
	6.18	1.53	0.17

VB_{onset} for dried and annealed samples as depicted in figure 5. These findings correspond well to the theoretical prediction of oxygen vacancy positioning (~1 eV above E_V) in a bridging site for bulk rutile SnO_2 [10].

As XPS analysis of deep and shallow core levels revealed differences in chemical composition between differently treated sol-gel SnO_x, in a next step, PYS examination of the band gap region below E_F was conducted. Figure 6(a) presents PY spectra for both kinds of samples. The low energy threshold of the $Y(E)$ spectrum allowed determination of the absolute value of E_F with respect to the vacuum energy level position $E_{vac} = 0$ eV, which, basing on its elementary definition, is the value of the work function φ [21]. Hence, $\varphi = 4.80$ eV and 4.65 eV were obtained for dried and annealed layers, respectively, manifesting work function reduction after thermal treatment. A similar work function decrease after an annealing process up to 1000 K in high-vacuum conditions was observed by Cox *et al* [13] for SnO_2 in UPS studies. In their work [13], annealing at temperature above 800 K led to creation of additional electronic defect states localized higher in the gap and was accompanied by significant increase of surface conductivity, likely induced by reduction. Cox *et al* [13] concluded that these intra-band gap states could be associated with surface rather than subsurface oxygen vacancies. Indeed, for our annealed samples which were also annealed to >800 K in ambient atmosphere, although substoichiometric, an increase of quantum yield near E_F was observed. This increase pointed to an increased density of occupied electronic states in this region in comparison to $Y(E)$ of dried samples (figure 6(a)).

In order to precisely analyse the distribution of occupied electronic states in the band gap below E_F, the effective density of filled states $N(E)$ was derived. Figures 6(b) and (c) display $N(E)$ curves for dried and annealed SnO_x, respectively, decomposed into particular components fitted with Gaussian peaks. Table 1 shows obtained peak positions, separately with respect to E_{vac} and E_F, and their FWHM, for both kinds of layers.

The obtained component positions confirmed an enhanced contribution of occupied electronic band gap states close to E_F

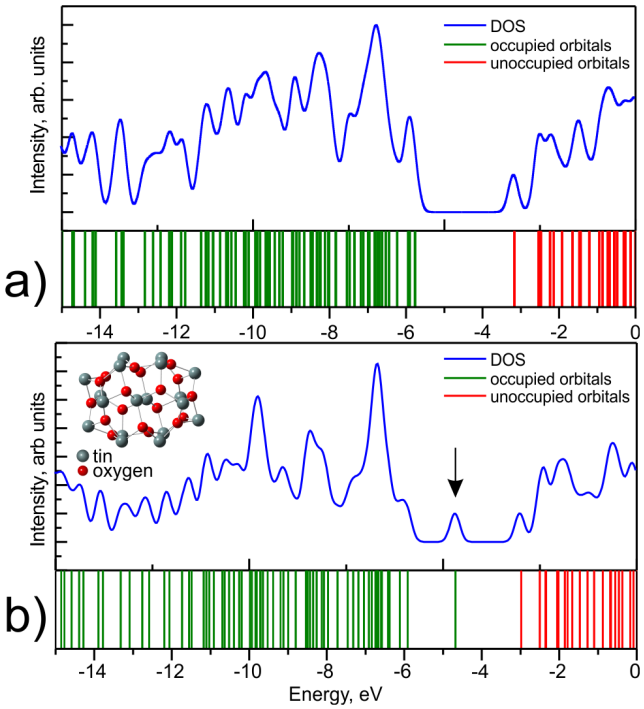

Figure 7. DOS calculation results of SnO_x electronic structure in the absence (a) and presence (b) of surface oxygen vacancies. Inset to panel (b) presents example of optimized SnO cluster. '0' on energy scale equalled to E_{vac}.

to the $N(E)$ curve. The enhancement is more pronounced for annealed layers. This result is evident especially in the absolute energy range 5.1 eV–5.4 eV, where an additional, wide peak with BE = 0.49 eV and FWHM = 0.40 eV was found (figure 6(c)). Following the above mentioned reasoning by Cox *et al*, the peak's origin was assigned to surface oxygen vacancies induced by the annealing process [13]. Moreover, energy positioning of these states is consistent with location of the highest occupied states at ~5.74 eV of absolute energy in DOS calculation of band structure by Trani *et al* for the $SnO_2(1\,1\,0)$ surface with oxygen vacancies at the outermost bridging site [14].

Increased intensities and widths of PYS-detected components for annealed SnO_x with respect to these for dried layers point out stronger impact of surface oxygen vacancies, in other words surface defect states, on electronic DOS within the band gap. It should be mentioned here that shallow core levels detected by XPS close to E_V roughly situated ~8 eV of absolute energy stemming from 'bridging' oxygen vacancies, have no contribution to the photoemission yield spectrum due to insufficient excitation energy of the incident photon applied in PYS.

The origin of additional shallow band gap states was verified utilising DOS semiempirical calculations. The SnO_x layers were modeled by a fragment of the tetragonal SnO bulk crystal as approximately corresponding to our experimental stoichiometry. In simulations, disturbance of oxygen amount was implemented by different number of O atoms (19 and 17) per Sn atoms (18). Two oxygen atoms were removed from the cluster surface modeling surface oxygen vacancies.

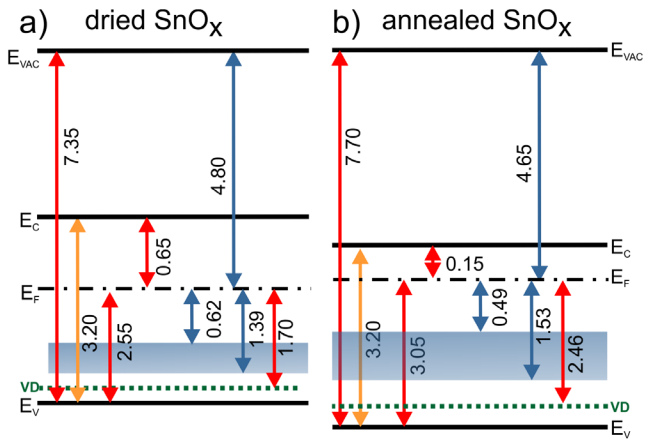

Figure 8. Energy level diagrams of spin-coated sol-gel SnO_x constructed for dried (a) and annealed (b) samples. All values are in eV and not drawn to scale. Red (■) arrows indicate electronic parameters obtained from XPS, blue (■) arrows stands for PYS data analysis and orange (■) arrows corresponds to values taken from literature [43]. The blueish (■) band represents the density of occupied electronic states obtained from the PYS spectrum, the green (■) dotted line—oxygen deficiency defect level detected in XPS.

Figures 7(a) and (b) shows the calculated theoretical DOS spectra for both cases. For structure with surface oxygen vacancies, a peak of additional occupied electronic states appears located inside band gap (figure 7(b)). Computed peak positioning close to 5 eV of absolute energy corresponds to location of experimentally detected in PYS defect electronic states and supported interpretation of their source.

It has to be said that although the computing methods often gives reasonable output [40], the cluster model used within these studies is a kind of minimalistic model hence obtained results shall be treated as supporting information.

To check the consistence of PYS-detected surface oxygen vacancy states with conductivity modification of the SnO_x layers, the negative charge carrier concentration n was calculated as [41] $n = N_c \cdot \exp[-(E_c - E_F)/kT]$, where N_c is the effective DOS in the conduction band, equaling $2 \cdot \left(2 \cdot m_e^* kT/h^2\right)^{3/2}$. The quantity m_e^* is the effective electron mass in the state, for SnO_2 established as 0.3 in unit of the free electron mass m_0 [42]. As usual, k is the Boltzmann constant, T the absolute temperature, here $T = 300$ K, and h the Planck constant. The energy distance $E_c - E_F$ was taken as the difference between width of band gap and $E_V - E_F$ previously determined from XPS of the VB region. For E_g, a value of 3.2 eV [43] was used, lower than for pure stoichiometric SnO_2 [5], but reasonable for reduced tin oxide. As a result, $n \sim 4 \cdot 10^{14}$ m^{-3} and $\sim 8 \cdot 10^{22}$ m^{-3} were obtained for dried and annealed layers, respectively. It should be noted that the significant difference in calculated n for both layers should be treated as only qualitative, because of underestimations of different other factors affecting the total concentration of carriers, such as the impact of surface band bending [1]. Nevertheless, the obtained n indicates a significant increase of charge carrier concentration after post-deposition annealing. This result agrees with findings of Cox *et al*, where the appearance of surface oxygen vacancies intra-gap states was associated with increase of surface conductivity [13].

The effect of n tuning related to post-deposition process was also observed by Rana *et al* [44, 45] for sol-gel spin-coated Sb-doped SnO_2 films subjected to swift heavy ions (SHI) irradiation. There, surface morphological features towards amorphization and lattice distortion were induced by SHI influence, and mirrored in increased RMS roughness parameter from 1.3 nm for pristine layer to 3.4 nm for an irradiated one. In result, lowering of n value was reported due to induced acceptor type defects which trapped the free electrons [44, 45]. The authors emphasise that modified grain boundaries and ionised defects present on the surface could scatter the carriers and finally affect electron transport in TCO [44, 45]. An analogue effect was observed by Gautam *et al* for Nb-doped TiO_2 when SHI irradiation produced defects in the lattice which implied a transformation of orbital character of O 2p and Ti 3d unoccupied states in the conduction band and creation of shallow or deep band gap states shifting the Fermi level [46]. This point of view is consistent with microscopic and photoelectron results for SnO_x samples in this work, especially for the dried sample. The dried layer possesses, on the one hand, an amorphous surface having greater RMS roughness, i.e. enhanced number of lattice defects, and on the other hand, the lower carrier concentration with respect to annealed layer.

Compiling all determined electronic parameters for dried and annealed layers allowed the construction of band diagrams as shown in figure 8. The diagrams visualise the layers' electronic structure and the impact of post-deposition treatment of sol-gel prepared tin oxide on Fermi level position relative to bottom of conduction band, as well as modification of location and density of additional occupied electronic states in the band gap. As a consequence, they manifest that drying and annealing process can reduce or augment the n-type character of SnO_x thus tailoring the layers for different particular applications.

Summary

Within the presented work, we show the post-deposition thermal processing, i.e. drying and annealing, impact on the structural, chemical and electronic properties of the sol-gel synthesized spin-coated SnO_x layers. Dried SnO_x layers ($x = 1.03$) exhibited amorphous topography and morphology as checked with XRD, SEM with moderately developed surface of roughness of the order of 6.3 nm determined by AFM technique.

The annealed SnO_x ($x = 1.08$) samples, although exhibiting lower roughness (4.4 nm) consisted of mixture of SnO_2 and SnO crystallographic phases which was reflected in surface topography presenting uniform distribution of small but distinct nano-sized grains.

Further process-induced alterations, like changes in chemical composition and stoichiometry, electronic properties and density of occupied states were obtained by complementary photoemission techniques, XPS and PYS. XPS examinations of O 1s and Sn $3d_{5/2}$ core levels revealed species corresponding to

tin valency Sn^{2+} and Sn^{4+} for both kinds of layers, with stronger contribution of SnO-like environment for dried SnO_x. Next, the VB XPS region examination revealed O 2p and Sn 5p/5s–O 2p hybridised states which was used for the top of the VB determination. In the band gap region, XPS spectra exhibited an additional peak resulting from deep band gap emission of Sn 5s electrons overlapping with the low BE tail of the O 2p signal. This contribution was assigned to increased presence of Sn^{2+} cations in the dried layers and as an origin of these occupied defect states, the 'bridging' oxygen vacancies were indicated.

Further PYS studies revealed the impact of post-deposition treatment on SnO_x electronic structure within the band gap region below E_F. The enhanced effective density of occupied electronic states near E_F position in case of annealed layers was found resulting in significantly higher charge carrier concentration. These states were reflected in a work function reduction from 4.80 eV for dried samples to 4.65 eV for annealed SnO_x. The origin of these shallow band gap states was concluded to be the presence of surface oxygen vacancies at the outermost bridging site, as confirmed by semiempirical DOS calculations.

In conclusion, simple and cost effective sol-gel technology followed by easy spin-coat deposition technique yields extremely oxygen-deficient tin oxide layers. Post-deposition treatment can significantly modify the layer's electronic structure, resulting e.g. in strong increase of conductivity, deepening n-type character of the synthesized SnO_x after annaling. We demonstrated that subtle treatment could be used to tailor the material to particular needs as well we showed that a set of laboratory—based photoemission techniques with different excitation ranges can be an effective tool for detailed layer characterisation.

Acknowledgments

This work was partially supported by the Polish budget for science through the Ministry for Science and Higher Education within Iuventus Plus IP2012 019072 project. L G would like to acknowledge assistance of the Institute of Physics—CSE through statutory funds BK-229/RIF/2017. A S and A E are grateful for support from the Max Planck Society through Maxnet Energy. Authors acknowledge the ESPEFUM laboratory at the Institute of Physics—CSE, Silesian University of Technology for access to the PYS experimental setup. Special thanks go to Professor Jerzy Bodzenta and Professor Andrzej Bluszcz for support. Open Access funding provided by the Max Planck Society.

ORCID iDs

Maciej Krzywiecki https://orcid.org/0000-0002-6151-8810

References

[1] Batzill M and Diebold U 2005 *Prog. Surf. Sci.* **79** 47
[2] Wicker S, Guiltat M, Weimar U, Hemeryck A and Barsan N 2017 *J. Phys. Chem.* C **121** 25064
[3] Komolov A S, Lazneva E F, Gerasimova N B, Zimina M V, Si P and Panina Y A 2015 *Phys. Solid State* **57** 2550
[4] Lahlalia A, Filipovic L and Selberherr S 2018 *IEEE Sens. J.* **18** 1
[5] Tsuda N 2000 *Electronic Conduction in Oxides* (Berlin: Springer)
[6] Hosono H, Ogo Y, Yanagi H and Kamiya T 2011 *Electrochem. Solid-State Lett.* **14** H13
[7] Krzywiecki M, Sarfraz A and Erbe A 2015 *Appl. Phys. Lett.* **107** 231601
[8] Kumar V, Kumar V, Som S, Neethling J H, Olivier E, Ntwaeaborwa O M and Swart H C 2014 *Nanotechnology* **25** 135701
[9] Kilic C and Zunger A 2002 *Phys. Rev. Lett.* **88** 095501
[10] Trani F, Causa M, Ninno D, Cantele G and Barone V 2008 *Phys. Rev.* B **77** 245410
[11] Varley J B, Schleife A, Janotti A and Van de Walle C G 2013 *Appl. Phys. Lett.* **103** 082118
[12] Themlin J M, Chtaib M, Henrard L, Lambin P, Darville J and Gilles J-M 1992 *Phys. Rev.* B **46** 2460
[13] Cox D F, Fryberger T B and Semancik S 1988 *Phys. Rev.* B **38** 2072
[14] Themlin J M, Sporken R, Darville J, Caudano R, Gilles J M and Johnson R L 1990 *Phys. Rev.* B **42** 11914
[15] Orgo Y, Hiramatsu H, Nomura K, Yanagi H, Kamiya T, Hirano M and Hosono H 2008 *Appl. Phys. Lett.* **93** 032113
[16] Le T, Dang H P, Luc Q H and Le V H 2017 *J. Phys. D: Appl. Phys.* **50** 145102
[17] Kwoka M, Ottaviano L, Koscielniak P and Szuber J 2014 *Nanoscale Res. Lett.* **9** 260
[18] Sberveglieri G 1995 *Sensors Actuators* B **23** 103
[19] Kwoka M and Krzywiecki M 2015 *Mater. Lett.* **154** 1
[20] Kanai K, Honda M, Ishii H, Ouchi Y and Seki K 2012 *Org. Electron.* **13** 309
[21] Ishii H, Kudo K, Nakayama T and Ueno N 2015 *Electronic Processes in Organic Electronics* (Tokyo: Springer)
[22] Grzadziel L and Krzywiecki M 2014 *Thin Solid Films* **550** 361
[23] Krzywiecki M, Grzadziel L, Sarfraz A and Erbe A 2017 *Phys. Chem. Chem. Phys.* **19** 11816
[24] Fernandez R, Gomez-Rodriguez J M, Colchero J, Gomez-Herrero J and Baro A M 2007 *Rev. Sci. Instrum.* **78** 013705
[25] www.casaxps.com
[26] Frisch M J *et al* 2004 Gaussian 03 Revision C.01. (Wallingford, CT)
[27] O'Boyle N M and Vos J G 2005 GaussSum 3.0 (Dublin City University)
[28] Kim S P, Choi M Y and Choi H C 2016 *Mater. Res. Bull.* **74** 85
[29] Santhi K, Rani C and Karuppuchamy S 2016 *J. Alloys Compd.* **662** 102
[30] Hsu P-C, Chen W-C, Tsai Y-T, Kung Y-C, Chang C-H, Wu C-C and Hsieh H-H 2014 *Thin Solid Films* **555** 57
[31] Kim I H, Ko J H, Kim D, Lee K S, Lee T S, Jeong J-H, Cheong B, Baik Y-J and Kim W M 2006 *Thin Solid Films* **515** 2475
[32] Kim S E-K and Oliver M 2010 *Met. Mater. Int.* **16** 441
[33] Giulio M D, Manno D, Micocci G, Rella R, Siciliano P and Tepore A 1993 *Sol. Energy Mater. Sol. Cells* **31** 235
[34] Weidner M, Jia J, Shigesato Y and Klein A 2016 *Phys. Status Solidi* B **253** 923
[35] Sivasankar Reddy A, Figueiredo N M and Cavaleiro A 2012 *Vacuum* **86** 1323
[36] Cittadini M, Bersani M, Perrozi F, Ottaviano L, Wlodarski W and Martucci A 2014 *Carbon* **69** 452
[37] Li D, Gong Y, Zhang Y, Luo C, Li W, Fu Q and Pan C 2015 *Sci. Rep.* **5** 12903

[38] Wang Y, Wang B, Lei Y, Wu N, Han C, Gau Y and Fang D 2015 *Appl. Surf. Sci.* **335** 208
[39] Walls J M and Smith R 2013 *Surface Science Techniques* (Oxford: Elsevier)
[40] Causa M, Pavone M, Trani F and Barone V 2005 *Nuovo Cimento* B **123** 1381
[41] Monch W 1995 *Semiconductor Surfaces and Interfaces* (Berlin: Springer)
[42] Rodl C and Schleife A 2014 *Phys. Status Solidi* A **211** 74
[43] Liu X, Zheng H, Zhang J, Xiao Y and Wang Z 2013 *J. Mater. Chem.* A **1** 10703
[44] Rana M P S, Singh F, Negi S, Gautam S K, Singh R G and Ramola R C 2016 *Ceram. Int.* **42** 5932
[45] Rana M P S, Singh F, Joshi K, Negi S and Ramola R C 2016 *Thin Solid Films* **616** 34
[46] Gautam S K, Das A, Ojha S, Shukla D K, Phase D M and Singh F 2016 *Phys. Chem. Chem. Phys.* **18** 3618